

Quantum reaction dynamics of $O(^3P)+HCl$ on a new *ab initio* potential energy surface

Katsuyuki Nobusada^{a)}

Division of Chemistry, Graduate School of Science, Hokkaido University, Sapporo,
Hokkaido 060-0810, Japan

Hiroki Nakamura

Department of Theoretical Studies, Institute for Molecular Science, Myodaiji, Okazaki 444-8585, Japan

Yongjing Lin and B. Ramachandran

Chemistry, College of Engineering and Science, Louisiana Tech University, Ruston, Louisiana 71272

(Received 20 March 2000; accepted 19 April 2000)

Quantum reaction dynamics of $O(^3P)+HCl \leftrightarrow OH+Cl$ is studied by using a new *ab initio* potential energy surface calculated by Ramachandran *et al.* [J. Chem. Phys. **111**, 3862 (1999)]. The hyperspherical *elliptic* coordinate approach is applied with an emphasis on elucidating reaction dynamics for J (total angular momentum quantum number)=0. In terms of the previously established concept that reactive transitions are nothing but vibrationally nonadiabatic transitions at important avoided crossings, clear interpretations are given for the following dynamical features: (i) reactivity depending on potential energy surface topography, (ii) final rotational state distributions for specified initial rovibrational states, and (iii) resonance structures appearing in some reactions. Thermal rate constants are approximately estimated from the present $J=0$ results by using the J -shift approximation. The present results are compared with our previous ones based on the different potential energy surface calculated by Koizumi–Schatz–Gordon (KSG). The calculated adiabatic potential energy curves of the present new surface have deep wells in the $OH+Cl$ channel in contrast to the KSG potential energy surface. Consequently, the new surface leads to quite different dynamics from those on the KSG surface. Comparisons with the results obtained by quasiclassical trajectory calculations are also made. © 2000 American Institute of Physics. [S0021-9606(00)01227-7]

I. INTRODUCTION

In a series of our recent studies of quantum reaction dynamics of the heavy–light–heavy (HLH) triatomic systems, we have developed a new numerical method and established a basic concept to elucidate the reaction mechanisms.^{1–5} The numerical method is based on the hyperspherical elliptic coordinates developed by Tolstikhin *et al.*⁶ This coordinate system is different from the conventional Delves⁷ type and Smith–Whitten⁸-type hyperspherical coordinate systems. The two hyperangles ξ and η in the hyperspherical elliptic coordinates well represent the vibrational and rotational motions, respectively, in HLH systems.^{1,2} This good separability is not only favorable for numerical calculations but also very useful for clarifying the reaction dynamics qualitatively.^{2–5} Making use of this big advantage, we have successfully introduced vibrationally adiabatic potential ridges and conceptualized electronically adiabatic chemical reactions as vibrational nonadiabatic transitions at avoided crossings in the vicinity of the ridges. The ridge line in collinear reactions can be clearly defined and presents a generalized concept of the transition state.⁹ In the previous studies, we have demonstrated that the ridge lines in mathematically three-dimensional reactive systems are defined by assuming

the vibrational adiabaticity within the hyperspherical elliptic coordinate approach, and the lowest ridge line corresponding to the ground vibrational state nicely represents the boundary of reaction zone. In any reactive systems studied, the reaction mechanisms can be qualitatively clarified by analyzing nonadiabatic transitions at a few important avoided crossings in the vicinity of the ridge line.

So far, we have applied the above approach to an example of almost isoergic reactions, i.e., $O(^3P)+HCl$,^{2,3} an example of symmetric systems, i.e., $Cl+HCl$,⁴ and an example of asymmetric exo- (or endo-)ergic systems, i.e., $Cl+HBr$.⁵ For example, in the case of $O(^3P)+HCl \rightarrow OH+Cl$, we have used the London–Eyring–Polanyi–Sato (LEPS)¹⁰ and the Koizumi–Schatz–Gordon (KSG)¹¹ potential energy surfaces (PES). The following dynamical features have been clarified: (i) onset of reaction for a specified initial rovibrational state, and (ii) major reactive transitions for a specified initial rovibrational state. Although the KSG-PES is an *ab initio* surface, it contains some defects basically due to the fitting procedure.²

Recently, Ramachandran *et al.* carried out *ab initio* calculations of the same reactive system at the multireference (single double) configuration interaction [MR-(SD)CI]/cc-pVTZ level of theory, using full-valence complete active space self-consistent field (CASSCF) wave functions as references.¹² These *ab initio* energies are expected to be

^{a)}Electronic mail: nobusada@sci.hokudai.ac.jp

more accurate than the MP2/6-31G(d,p) calculations of KSG.¹¹ The Davidson-corrected MR-(SD)CI energies [MR-(SD)CI+Q] were scaled using the scaled external correlation (SEC) method of Brown and Truhlar¹³ and fitted to a simple analytic expression. Different fits, named S1, S1A, S2, and S4, were generated which differ from each other in the choice of the SEC scaling factor and the choice of models for the asymptotic diatomic potentials.^{12,14,15} The most recent of these fits, namely the S4 surface, was used for a fairly extensive quasiclassical trajectory simulation of the state-to-state integral cross-section experiments of the Zare group¹⁶ and was found to reproduce many of the experimental observations satisfactorily.^{15,17} Although a time-dependent quantum-mechanical study has been carried out on the S2 surface,¹⁸ and time-dependent studies on the S4 surface are forthcoming,^{19,20} discussions of the reaction mechanism on the S4 surface based on our aforementioned concept, or studies of the reverse reaction, have not yet been done.

In this paper, we apply our approach to the reactive system of $O(^3P)+HCl \leftrightarrow OH+Cl$ with use of the new *ab initio* potential surface S4 and clarify the reaction dynamics qualitatively. Differences in reaction dynamics of the two surfaces S4 and KSG are discussed from a viewpoint of the potential energy surface topography. The vibrational adiabatic potential energy curves calculated from the S4-PES show shallow and deep potential wells in the reactant ($O+HCl$) and the product ($OH+Cl$) channels, respectively, in sharp contrast to the KSG-PES. These characteristic features of the S4-PES cause new interesting features as follows: (i) Reactivity is quite different from that of the KSG-PES strongly depending on the initial rovibrational states. In particular, the reverse reaction $OH+Cl \rightarrow O+HCl$ is very much suppressed for low rotational states. (ii) Feshbach resonances show up conspicuously. All these dynamical features are interpreted in terms of nonadiabatic transitions at important avoided crossings. Since the present calculations are carried out only for J (total angular momentum quantum number)=0, we cannot obtain accurate reaction cross sections and rate constants. Although the so-called J -shift approximation²¹ is frequently used to estimate $J \neq 0$ reaction probabilities, it should be noted that the simple J -shift approximation does not always work well and various improvements have been attempted.²²⁻²⁴ Nevertheless, since the standard J -shift approximation can give reasonable results within a factor of 2 or so for thermal rate constant at low temperatures, here we simply use this approximation to roughly estimate the thermal rate constants.

We have also carried out two types of quasiclassical trajectory (QCT) calculations, the results of which are compared to the quantum results where applicable. One type of trajectory calculations yields reaction probabilities for $J=0$, and provides interesting comparisons to analogous quantum-mechanical reaction probabilities. Another type of trajectory calculation samples all possible values of J in a statistical manner and yields reaction cross sections which are then used to calculate QCT rate constants as a function of temperature. The thermal rate constants thus obtained are compared to the quantum rate constants obtained by the J -shift approximation.

This paper is organized as follows. In the next section,

we briefly summarize the method of quantum-mechanical calculations based on the hyperspherical elliptic coordinates and explain our basic idea to elucidate reaction dynamics. The global characteristics of the adiabatic potential energy curves are mentioned in the section. A brief outline of the QCT calculations is also given. In Sec. III, results of the accurate quantum-mechanical calculations are reported for $J=0$. The detailed mechanisms of the reaction are clarified. The quantum-mechanical results for the S4-PES are compared to the previous ones for the KSG-PES and also the present QCT ones. Concluding remarks are given in Sec. IV.

II. METHOD OF QUANTUM AND CLASSICAL DYNAMICS CALCULATIONS

The present quantum numerical method based on the hyperspherical elliptic coordinates and the basic idea to elucidate reaction dynamics have been previously described in detail.^{1,2} Here, we give only a brief review. The coordinate system consists of the hyper-radius ρ and the hyperspherical elliptic angles (ξ, η) to parametrize the hypersphere. Using these coordinates, the Schrödinger equation for $J=0$ is given by

$$[K(\rho) + H_{\text{ad}}(\xi, \eta; \rho) - \mu\rho^2 E] \Psi(\rho, \xi, \eta) = 0, \quad (1)$$

where $K(\rho)$ represents the kinetic energy for the motion in ρ , H_{ad} is the adiabatic Hamiltonian defined at fixed ρ which is composed of the angular kinetic energy and the interaction potential, μ is the characteristic mass, and E is the total energy measured from the ground rovibrational state of the reactant HCl (i.e., 0.183 eV higher than the bottom of the HCl potential). The adiabatic potentials $U_\nu(\rho)$ and the channel eigenfunctions $\Phi_\nu(\xi, \eta; \rho)$ are obtained by solving the following eigenvalue problem:

$$[H_{\text{ad}}(\xi, \eta; \rho) - \mu\rho^2 U_\nu(\rho)] \Phi_\nu(\xi, \eta; \rho) = 0, \quad (2)$$

where ν indicates the adiabatic channel number. This is a mathematically two-dimensional eigenvalue problem and is efficiently solved by taking advantage of the good separability of the hyperspherical elliptic angles ξ and η in the HLH systems.^{1,2} Equation (2) is first solved with respect to the ξ motion, which well represents the vibrational motion of both reactant and product, and then with respect to the η motion. After solving the eigenvalue problem with respect to ξ , we obtain the vibrationally adiabatic potentials for each vibrational quantum state of n_ξ as a function of η . The potential ridge line for each n_ξ is drawn as a function of ρ by projecting the barrier top of the corresponding vibrationally adiabatic potential.² When solving Eqs. (1) and (2), we use the slow-variable-representation method.²⁵ The differential equation with respect to ρ in Eq. (1) is solved by using the R -matrix propagation method.²⁶ After imposing a proper scattering boundary condition on $\Psi(\rho, \xi, \eta)$ in the asymptotic region, the scattering matrix is finally obtained.

In the present calculations, we use the new *ab initio* potential energy surface S4 developed by Ramachandran *et al.*¹⁵ They have carried out several calculations^{12,14} and proposed this final best analytical function fitted to their best *ab initio* data.¹⁵ Figure 1 shows the adiabatic potential curves calculated from the S4-PES. The broken line indicates the

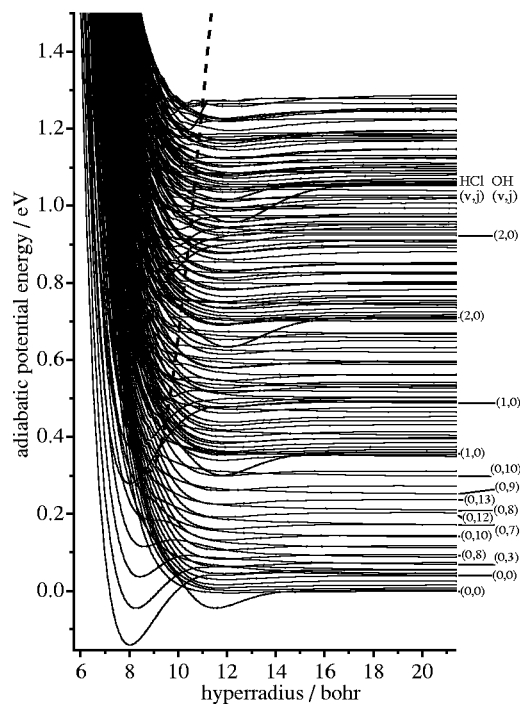


FIG. 1. Adiabatic potential energy curves of the new *ab initio* potential energy surface. The broken line is the $n_{\xi}=0$ potential ridge line. Some representative rovibrational quantum numbers of HCl and OH are indicated at the right edge.

$n_{\xi}=0$ potential ridge line as mentioned above. Several representative rovibrational states of HCl and OH are indicated at the right edge. As is clearly seen from the figure, the present adiabatic potential curves are quite different from those of KSG (see Fig. 6 in Ref. 2). In particular, the present adiabatic potential curves have two different types of wells, i.e., deep ones at $\rho \sim 8 a_0$ and relatively shallow ones at $\rho \sim 11.5 a_0$. The former reflects the deep potential well in the product OH+Cl channel of the S4-PES. The S4-PES actually has a potential minimum at $r_{\text{OH}}=1.90 a_0$, $r_{\text{HCl}}=4.12 a_0$, and $\angle \text{OHCl}=80.4^\circ$. These values in the Jacobi coordinates correspond to $\rho=7.98 a_0$. The S4-PES also has a potential minimum in the reactant O+HCl channel at $r_{\text{OH}}=3.83 a_0$, $r_{\text{HCl}}=2.46 a_0$, and $\angle \text{OHCl}=180^\circ$, which correspond to $\rho=11.49 a_0$. This minimum clearly corresponds to the shallow potential well in Fig. 1. As will be discussed later in detail, the above deep potential well at $\rho \sim 8 a_0$ causes some characteristic features which were completely absent in the case of the KSG-PES.

According to our basic idea,² reactive transitions (i.e., vibrationally nonadiabatic transitions) occur at some specific avoided crossings lying near the potential ridge line. Other avoided crossings appearing in the potential curve diagram are very sharp and nonadiabatic transitions do not occur effectively there. Therefore, we can elucidate major reaction dynamics by analyzing nonadiabatic transitions at important avoided crossings. This basic idea has actually been demonstrated to work well for various systems,²⁻⁵ and here we pursue the same idea.

The quasiclassical trajectory calculations are carried out using a modified version of Muckerman's program CLASTR,

which is based on the approach described in detail by Truhlar and Muckerman.^{27,28} The $J=0$ calculations are carried out by choosing the Cartesian components of orbital angular momentum \mathbf{l} so as to exactly cancel the components of the diatomic rotational angular momentum \mathbf{j} , thus yielding

$$\mathbf{J}=\mathbf{l}+\mathbf{j}=\hat{\mathbf{e}}_x(l_x+j_x)+\hat{\mathbf{e}}_y(l_y+j_y)+\hat{\mathbf{e}}_z(l_z+j_z)=0, \quad (3)$$

where the $\hat{\mathbf{e}}_x$ etc., are unit vectors pointing along the Cartesian axes. Since the total angular momentum is conserved during trajectory propagation, this restriction in the choice of initial conditions results in ensembles of trajectories for which the total angular momentum is zero to within the numerical precision of the integration procedure (typically better than 10^{-7}). To the best of our knowledge, this is the first report of QCT calculations for $j_i > 0$ where the total angular momentum J is restricted to zero. The details of initial state selection and the Monte Carlo sampling of phase space in these calculations will be published elsewhere. For each initial state, ensembles of 1000 trajectories are propagated at several collision energies. The results are presented below and compared to quantum reactive scattering results.

The classical reaction cross sections are obtained without restricting the angular momenta in any manner other than through the choice of b_{max} , which is chosen to be large enough so that trajectories with $b \geq b_{\text{max}}$ are unreactive. The reaction cross sections for $v=0$ are obtained by propagating ensembles of 10 000 trajectories at several collision energies in the energy range $0.0 \leq E_{\text{coll}} \leq 0.87$ eV for states with $j_i = 0, 1, \dots, 20$. The reaction cross sections for $v_i=1$ are obtained as a function of temperature by propagating 10 000 trajectories at each temperature, where the initial rotational quantum number for each trajectory is chosen from a Boltzmann distribution.²⁹ These cross sections are used to obtain thermal rate constants as a function of temperature by the usual methods.^{28,30}

III. RESULTS AND DISCUSSIONS

A. Cumulative and state-to-all reaction probabilities

The total cumulative reaction probabilities (CRP) and the vibrationally specified CRPs as a function of the total energy are shown in Fig. 2. In these figures, the origin of the energy axis corresponds to the asymptotic zero-point energy of the $\text{O}(^3P)+\text{HCl}$ arrangement. The solid lines are the present results and the broken lines are those obtained by using the KSG-PES. As is clearly seen from these figures, the disagreement between the two PESs is quite large. The reaction probabilities for S4 are generally larger than those for KSG and have more structures. The vibrationally adiabatic reaction barrier, $\Delta V_{\text{zpe}}^\ddagger$, (taking into account the zero-point energies of the reactant and the transition state) is 0.35 eV on the S4 surface and 0.29 eV on the KSG surface.¹⁵ Therefore, the quantum reaction probability for $E \leq \Delta V_{\text{zpe}}^\ddagger$ is due to the tunneling of the H atom. It is clear that the S4 surface permits considerably more tunneling than the KSG surface. It will be shown below that this property of the S4 surface has a significant influence on the thermal rate constants at low temperature.

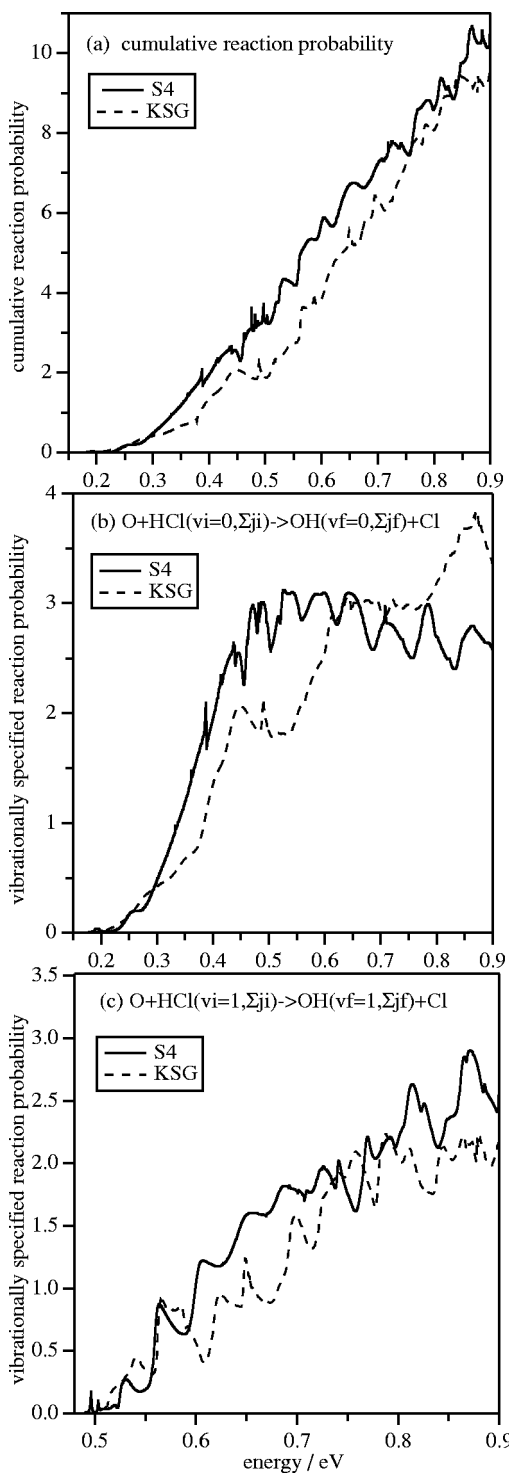


FIG. 2. Total and vibrationally specified cumulative reaction probabilities as a function of the total energy. The solid lines indicate the present results and the broken ones the results for the KSG-PES.

Figure 3 show the state-to-all reaction probabilities for (a) $O+HCl(v_i=0, j_i=0, 7) \rightarrow OH(v_f=0, \Sigma_{j_f})+Cl$, and (b) $OH(v_i=0, j_i=0, 7)+Cl \rightarrow O+HCl(v_f=0, \Sigma_{j_f})$. The disagreement between the two PESs becomes much larger. In Fig. 3(a), both ($j_i=0$ and 7) reaction probabilities for S4 are larger than the corresponding probabilities for KSG and have sharp peaks. Interestingly, the reverse reaction $OH+Cl \rightarrow O+HCl$ for $j_i=0$ on the S4-PES is very much suppressed

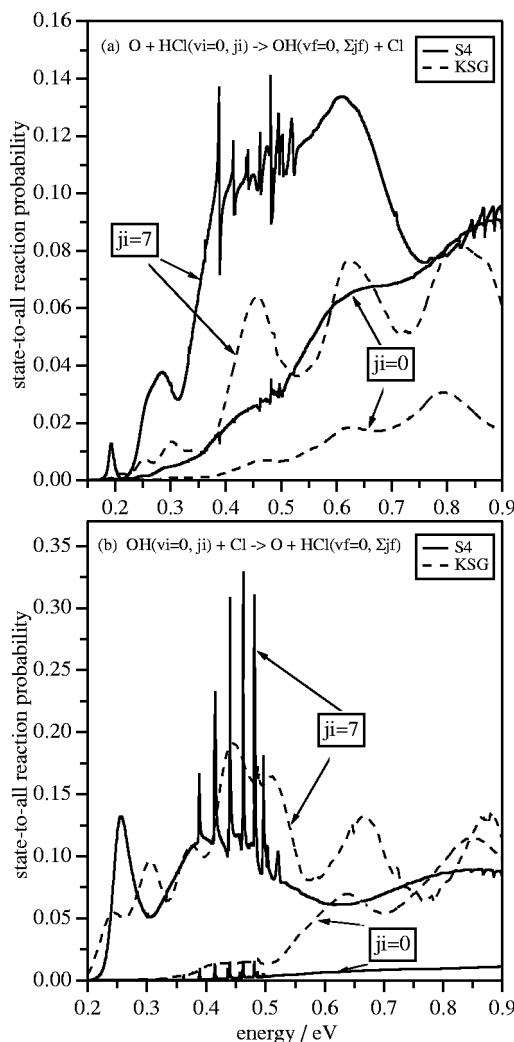


FIG. 3. State-to-all reaction probabilities for (a) $O+HCl(v_i=0, j_i=0, 7) \rightarrow OH(v_f=0, \Sigma_{j_f})+Cl$, and (b) $OH(v_i=0, j_i=0, 7)+Cl \rightarrow O+HCl(v_f=0, \Sigma_{j_f})$ as a function of the total energy. The solid lines indicate the present results and the broken ones the results for the KSG-PES.

in the wide energy range. However, the reverse reaction for $j_i=7$ on the S4-PES occurs comparably to the reaction on the KSG-PES. Furthermore, the probabilities for the S4-PES show sharp peaks as well as in the case of $O+HCl \rightarrow OH+Cl$. These features can be well understood with the help of the adiabatic potential energy curves. We first explain the different reactivity depending on the surfaces. The origin of the peaks will be discussed later.

Let us follow the potential energy curve asymptotically correlating to $OH(v=0, j=0)$ in Fig. 1. It is better to see Fig. 4, which is the magnification of Fig. 1. The curve encounters several avoided crossings at $\rho \gtrsim 10a_0$, at which we can follow diabatically because the avoided crossings are far from the potential ridge line and are so sharp that no effective nonadiabatic transitions occur there. (The way to follow adiabatic potential curves near avoided crossings has been described in our previous paper in detail.² A much more accurate semiclassical treatment of avoided crossings is presented in Ref. 31 by Zhu *et al.*) As a result of this, we end up with the lowest potential curve at $\rho \lesssim 10a_0$ which has a deep well at $\rho \sim 8a_0$. This adiabatic potential curve does not have

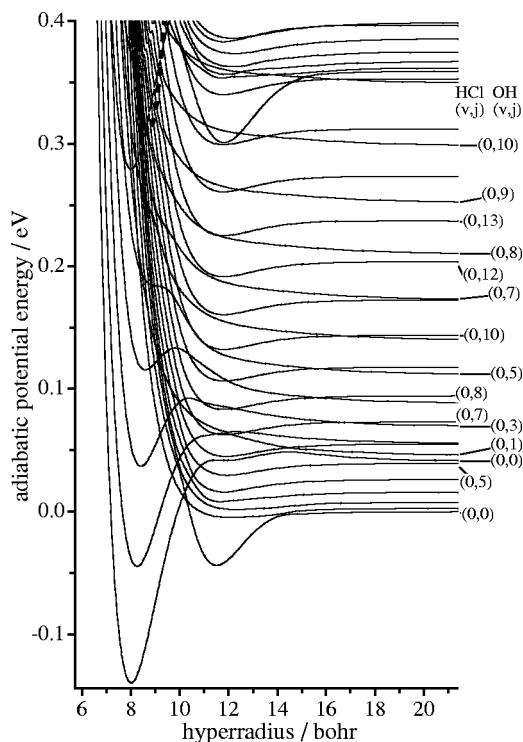


FIG. 4. Magnification of the adiabatic potential energy curves of Fig. 1 below $E \leq 0.4$ eV.

any effective avoided crossings at $\rho \leq 8a_0$. Therefore, even at high energies like $E \sim 0.9$ eV no effective nonadiabatic transitions occur along this diabatically connected potential curve. This is the reason why the reverse reaction for OH ($v_i=0, j_i=0$) + Cl \rightarrow O + HCl ($v_f=0, \Sigma j_f$) is strongly suppressed on the S4-PES as shown in Fig. 3(b). On the contrary, in the case of the KSG-PES the potential curve which correlates to OH ($v=0, j=0$) goes up diabatically and reaches the reaction zone bounded by the $n_\xi=0$ ridge line (see Fig. 6 in Ref. 2). Thus, the reaction for OH ($v_i=0, j_i=0$) + Cl \rightarrow O + HCl ($v_f=0, \Sigma j_f$) occurs more effectively on the KSG-PES. Figure 3(a), on the other hand, shows that the reaction of O + HCl ($v_i=0, j_i=0$) \rightarrow OH ($v_f=0, \Sigma j_f$) + Cl on the KSG-PES is relatively suppressed compared to that on the S4-PES. This is because the relevant potential curve of the KSG-PES [asymptotically correlating to HCl ($v=0, j=0$)] behaves in a way similar to the one correlating to OH ($v=0, j=0$) in the case of the S4-PES. In other words, the curve does not experience much effective avoided crossings. Finally, the reverse reaction probability for $j_i=7$ outstandingly increases on the S4-PES. Although the adiabatic potential energy curve asymptotically correlating to OH ($v=0, j=7$) on the S4-PES cannot be followed as easily as above; the curve actually encounters relatively much more effective avoided crossings near the ridge line. Therefore, the reverse reaction for $j_i=7$ occurs much more effectively than that for $j_i=0$.

As described above, the reactivities of the two PESs are quite different from each other strongly depending on the rovibrational states, and we may safely conclude that the cumulative reaction probability and thermal rate constants for the S4-PES are generally larger than those for the KSG-

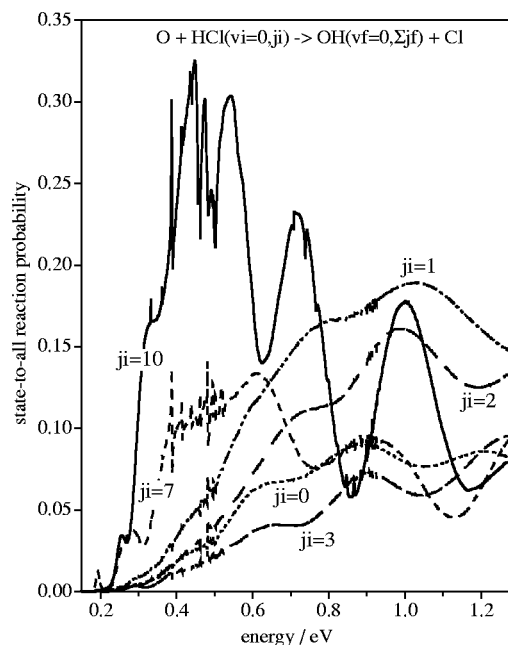


FIG. 5. State-to-all reaction probabilities for O + HCl ($v_i=0, j_i$) \rightarrow OH ($v_f=0, \Sigma j_f$) + Cl as a function of the total energy.

PES. It is interesting to note that in contrast to this fact, the barrier height at the saddle point of S4 is 1.28 kcal/mol higher than that of KSG.¹⁵ The high reactivity of the S4-PES in spite of the higher barrier may be ascribed to the fact that its barrier is much thinner than that of the KSG-PES. This is true for the overall reactivity at relatively low energies, but the detailed reaction dynamics in wide energy range is governed by a bit more global feature of the potential surface and actually by the above-mentioned concept of vibrationally nonadiabatic transitions at some important avoided crossings.

Figure 5 shows the state-to-all reaction ($\text{O} + \text{HCl}(v_i=0, j_i) \rightarrow \text{OH}(v_f=0, \Sigma j_f) + \text{Cl}$) probabilities for various j_i . The reaction probabilities become larger for $j_i=7$ and 10 at $E \leq 0.3$ eV. This is because the corresponding potential energy curves encounter effective avoided crossings lying near the potential ridge line. The reaction probabilities in Fig. 5 show resonance structures in the energy range of $0.33 \text{ eV} \leq E \leq 0.5 \text{ eV}$ and $0.7 \text{ eV} \leq E \leq 0.9 \text{ eV}$. This feature is more enhanced in the reverse reaction, OH + Cl \rightarrow O + HCl as shown in Fig. 6. It should be noted that the curves for $j_i=0$ and 7 in Figs. 5 and 6 are exactly the same as the curves in Fig. 3. As is clearly seen from Fig. 6, the resonance peaks appear at the same energies almost independently of j_i . The right-upper panel in Fig. 6 more clearly shows these resonance peaks. The peaks can be explained again by using the adiabatic potential energy curves. These are ascribed to Feshbach resonances supported by quasipotential wells appearing in Fig. 1 around $7.0 a_0 \leq \rho \leq 10.0 a_0$ and $0.3 \text{ eV} \leq E \leq 0.6 \text{ eV}$. Figure 7 is the magnification of the adiabatic potential energy curves in this region to show the quasipotential wells clearly. One of the quasipotential wells is drawn by a broken line by diabatically connecting adiabatic potentials. This quasipotential well is fitted by an analytical Morse function and its vibrational energy levels are calculated. Table I

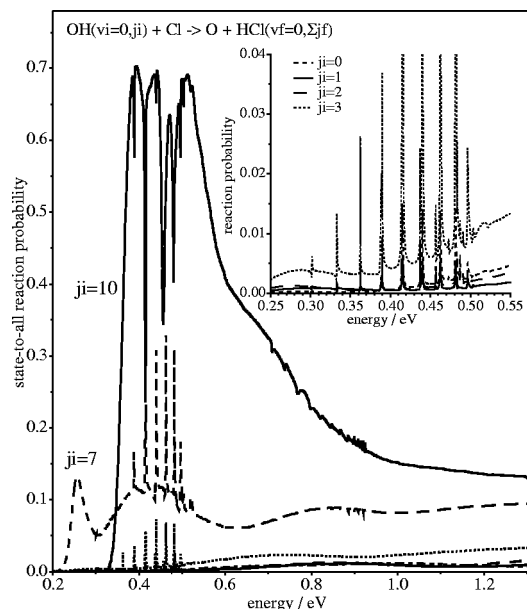


FIG. 6. State-to-all reaction probabilities for $OH(v_i=0, j_i=0-3,7,10)+Cl \rightarrow O+HCl(v_f=0, \Sigma j_f)$ as a function of the total energy. Magnification in the energy range of $0.25 \text{ eV} \leq E \leq 0.55 \text{ eV}$ is drawn in the right-upper panel.

shows the two Morse parameters and comparison between the Morse energy levels and the actual peak positions. The agreement is perfect up to $v=6$, indicating clearly that the peaks in Fig. 6 can be ascribed to the Feshbach resonances supported by the quasipotential well. The similar resonance peaks for $O+HCl \rightarrow OH+Cl$ appearing in the same energy range are also ascribed to the same Feshbach resonances. In Fig. 6, the resonance peaks become complicated at $E \geq 0.45 \text{ eV}$. This is because the different types of resonance peaks caused by two quasipotential wells are overlapped. The second quasipotential well is also clearly seen in Fig. 7 just above the first one.

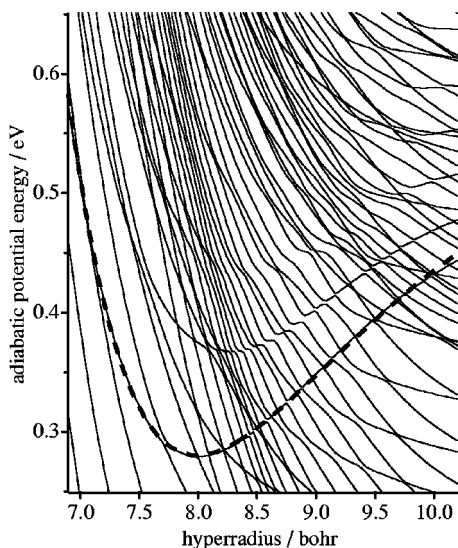


FIG. 7. Adiabatic potential energy curves magnifying Fig. 1 around $7.0 a_0 \leq \rho \leq 10.0 a_0$ and $0.25 \text{ eV} \leq E \leq 0.65 \text{ eV}$. The broken line represents the diabatically connected potential curve.

TABLE I. Two Morse parameters and vibrational energy levels of the Morse potential. The third column indicates actual peak positions.

Dissociation energy	0.29 52 eV	
exponential factor	0.640 784	
Vibrational quantum number	Energy level/eV	Peak position
0	0.3013	0.3019
1	0.3326	0.3332
2	0.3620	0.3624
3	0.3895	0.3896
4	0.4152	0.4151
5	0.4390	0.4402
6	0.4610	0.4626

We also compare the quantum and classical total CRPs [$O+HCl(\Sigma v_i, j_i) \rightarrow OH(\Sigma v_f, j_f)+Cl$] and initially vibrationally specified CRPs [$O+HCl(v_i=0,1, \Sigma j_i) \rightarrow OH(\Sigma v_f, j_f)+Cl$] for the S4-PES in Fig. 8(a). It is clear that although the classical probabilities lack the structures seen in the quantum probabilities, their relative magnitudes and shapes are remarkably similar. As noted already, the quantum probabilities include a significant tunneling component which is lacking in the case of the classical results. The agreement between the quantum and classical CRPs for $v=1$ shown in Fig. 8(a) is considerably better than that between the CRPs for $v=0$, presumably because the $v=1$ state lies above the reaction barrier and, therefore, threshold effects are less important. The agreement between the quantum and classical reaction probabilities out of individual rovibrational states of HCl are less impressive. However, as seen in Figs. 8(b) and 8(c), the qualitative agreement between the two improves considerably as the j quantum number increases.

B. State-to-state reaction probability and final rotational state distributions

In this section, we demonstrate that major state-to-state reactions and final rotational state distributions can also be understood in view of nonadiabatic transitions at important avoided crossings.

Figure 9 is an example of the state-to-state reactions, $O+HCl(v_i=0, j_i=13) \rightarrow OH(v_f=0, j_f)+Cl$. This figure shows that the major transition occurs from $j_i=13$ to $j_f=10$ at $E \approx 0.38 \text{ eV}$ and the secondary and tertiary peaks appear at $j_f=11$ and $j_f=12$, respectively. In order to comprehend the final rotational state distributions, we follow the potential energy curve in Fig. 4 correlating to $HCl(v=0, j=13)$ in the same way as before. The curve encounters a few sharp avoided crossings before reaching the ridge line, namely at $\rho \sim 11 a_0$ and $\rho \sim 9.7 a_0$. The important parameter a^2 to judge the significance of avoided crossing is more than 6000 at these avoided crossings. According to the semi-classical analysis,³¹ effective nonadiabatic transitions ($0.005 \leq p \leq 0.96$) occur in the range of $0.05 \leq a^2 < 100$. Thus, we can safely connect the potential curves diabatically. This potential curve finally encounters the avoided crossing at $\rho \approx 9.4 a_0$ just before the potential ridge line. This is an avoided crossing with the potential energy curve asymptotically and diabatically correlating to $OH(v=0, j=10)$. Since

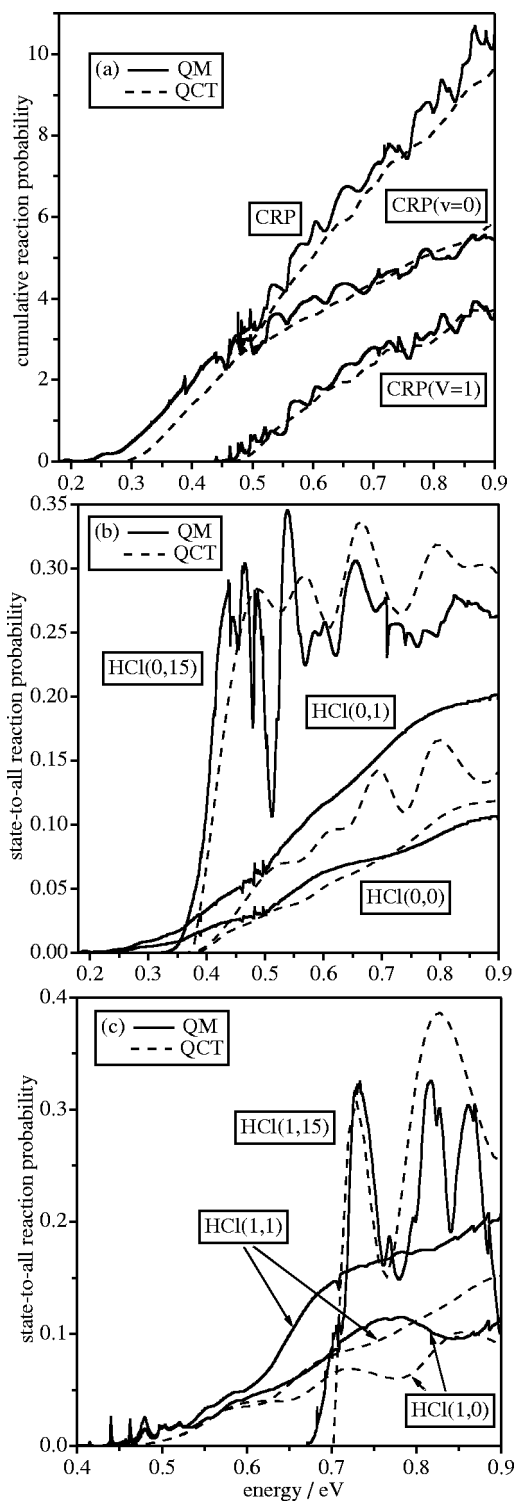


FIG. 8. Quantum and classical mechanical (a) total and initially vibrationally specified cumulative reaction probabilities, and (b), (c) state-to-all reaction probabilities for some representative initial rovibrational states. The solid lines are quantum-mechanical ones and broken lines classical ones.

this avoided crossing is located at the potential ridge line and the corresponding a^2 is actually ~ 22 , the nonadiabatic transition there occurs effectively. Therefore, the state-to-state reaction $\text{O} + \text{HCl}(v_i=0, j_i=13) \rightarrow \text{OH}(v_f=0, j_f=10) + \text{Cl}$ is expected to occur predominantly. As described previously,^{2,3} the inelastic rotational transitions easily occur before the reactive transitions. This causes the secondary and tertiary

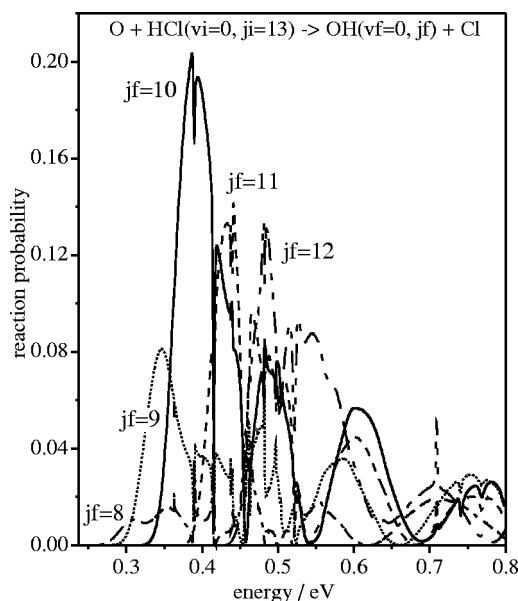


FIG. 9. Final rotational state distributions for $\text{HCl}(v_i, j_i) = (0,13)$ as a function of the total energy.

peaks of $j_f=11$ and 12 as shown in Fig. 9. Here, we have demonstrated only one example, but we have actually confirmed that major reaction processes can be comprehended in the same way.

C. Quantum and classical mechanical thermal rate constants

Since the present calculations are carried out only for $J=0$, we cannot obtain accurate rate constants. In order to approximately estimate the reaction probabilities for $J \neq 0$ from the $J=0$ results, the so-called J -shift approximation is frequently employed.²¹ As discussed in our previous paper²⁴ and by other authors,^{22,23} however, the standard J -shift approximation does not always work well. In particular, the approximation becomes worse with increasing energy, initial rovibrational states, or temperature. This is simply because higher $J \neq 0$ contribute predominantly to the reaction. In spite of the above-mentioned drawback, the standard J -shift approximation sometimes gives a reasonable estimate for a highly averaged quantity such as thermal rate constant.^{22–24} Thus, we have roughly estimated the thermal rate constants for the present reactive system using the standard J -shift approximation.

Figure 10 shows the thermal rate constants as a function of $1000/T$. For comparison, we have also plotted the quantum-mechanical thermal rate constants for the KSG-PES obtained under the J -shift approximation. Despite the fact that the two PESs show quite different reaction dynamics as described above, the two thermal rate constants agree well at low temperature, although the deviation between the two becomes noticeable with increasing temperature. This behavior is consistent with the fact that the cumulative reaction probabilities for the S4-PES become larger than those for the KSG-PES as the energy increases.

Even though we have used the simple J -shift approximation, we may say that the thermal rate constant for the S4-

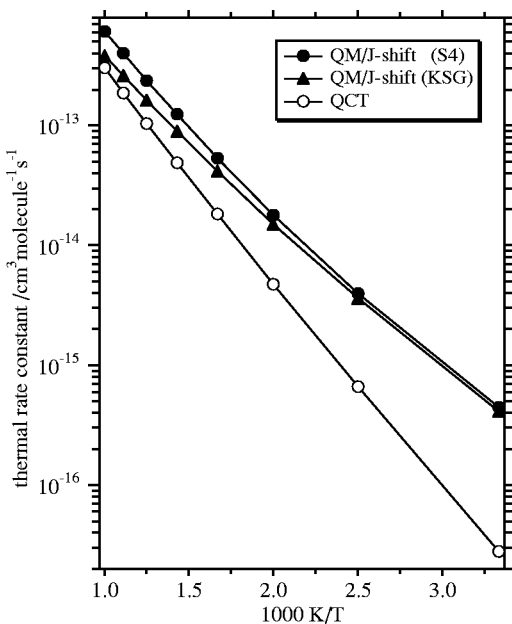


FIG. 10. Thermal rate constants as a function of $1000/T$. Closed circles and closed triangles are the J -shift approximated thermal rate constants for S4 and KSG, respectively. Open circles are the QCT thermal rate constants for S4.

PES is a bit too high in comparison with the experimental observations^{32–35} and thus we should further improve the accuracy of the potential energy surface. Figure 10 shows also the result of the QCT calculations, which is too low especially at low temperatures. This is clearly due to the tunneling effect.

IV. CONCLUDING REMARKS

We have studied quantum reaction dynamics of $O(^3P)+HCl \leftrightarrow OH+Cl$ by using the new *ab initio* potential energy surface S4. The reaction dynamics is qualitatively well interpreted in terms of our previously established basic concept that reactive transitions are regarded as vibrationally nonadiabatic transitions at important avoided crossings. Examples are (i) reactivity depending on the initial rovibrational states, (ii) major part of final rotational state distributions for an initially specified rovibrational state, and (iii) resonance structures, which are ascribed to Feshbach resonances supported by diabatically connected quasipotential wells. The present results are compared to our previous results based on the different potential energy surface termed as KSG. The potential energy surface topographies of the two PESs are quite different from each other. Actually, the reaction dynamics has been found to sensitively depend on the differences of the potential surfaces as follows: (i) The cumulative reaction probabilities are generally larger for the S4-PES than for the KSG-PES. (ii) The reactivity of state-resolved reaction strongly depends on the initial rovibrational state. In particular, the reverse reaction $OH(v_i=0, j_i \sim 0-3)+Cl \rightarrow O+HCl$ on the S4-PES is strongly suppressed because of the absence of important avoided crossings. (iii) The deep potential well appearing in the adiabatic potential energy curves of the S4-PES causes interesting resonance

structures. These resonance structures, which are completely absent in the case of the KSG-PES, are ascribed to Feshbach resonances as mentioned above.

The thermal rate constants were roughly estimated within the J -shift approximation for both surfaces of S4 and KSG. At lower temperature, the two rate constants agree with each other in spite of the big difference of the potential energy surface topography. However, the deviation becomes large with increasing temperature, reflecting the fact that the reactivity on the S4-PES is generally larger than that on the KSG-PES with increasing energy. The quantum-mechanical results are also compared with those obtained by the QCT calculations. As expected, the classical method cannot give accurate results especially at low energies, at low temperatures, and for low rovibrational states. This is simply because the classical mechanics does not work well near the threshold energy. Furthermore, at present the S4-PES tunneling effect is relatively more important than in the KSG-PES. These are the reasons that the QCT thermal rate constants are much smaller than the quantum-mechanical ones at low temperature. However, the QCT reproduces relatively well the overall features of the reaction dynamics, except for the threshold region and the resonance structures. Unfortunately, the S4-PES leads to a thermal constant even higher than those of the KSG-PES and also the experimental observations. Further improvement is necessary for the potential surface of the present system.

ACKNOWLEDGMENTS

The authors would like to thank J. M. Bowman, S. K. Gray, and S. Nanbu for communicating their results to us. This work was partially supported by a Research Grant No. 10440179 and by a Grant-in-Aid for Scientific Research on Priority Area ‘‘Molecular Physical Chemistry’’ from The Ministry of Education, Science, Culture, and Sports of Japan. B.R.’s research was supported in part by the National Science Foundation of the United States, Grant No. CHE 97-12764.

- ¹O. I. Tolstikhin and H. Nakamura, *J. Chem. Phys.* **108**, 8899 (1998).
- ²K. Nobusada, O. I. Tolstikhin, and H. Nakamura, *J. Chem. Phys.* **108**, 8922 (1998).
- ³K. Nobusada, O. I. Tolstikhin, and H. Nakamura, *J. Phys. Chem. A* **102**, 9445 (1998).
- ⁴K. Nobusada, O. I. Tolstikhin, and H. Nakamura, *J. Mol. Struct.: THEOCHEM* **461–462**, 137 (1999).
- ⁵G. V. Mil’nikov, O. I. Tolstikhin, K. Nobusada, and H. Nakamura, *Phys. Chem. Chem. Phys.* **1**, 1159 (1999).
- ⁶O. I. Tolstikhin, S. Watanabe, and M. Matsuzawa, *Phys. Rev. Lett.* **74**, 3573 (1995).
- ⁷L. M. Delves, *Nucl. Phys.* **9**, 391 (1958/59); **20**, 275 (1960).
- ⁸F. T. Smith, *J. Math. Phys.* **3**, 735 (1962); R. C. Witten and F. T. Smith, *ibid.* **9**, 1103 (1968).
- ⁹A. Ohsaki and H. Nakamura, *Phys. Rep.* **187**, 1 (1990).
- ¹⁰A. Persky and M. Broida, *J. Chem. Phys.* **81**, 4352 (1984).
- ¹¹H. Koizumi, G. C. Schatz, and M. S. Gordon, *J. Chem. Phys.* **95**, 6421 (1991).
- ¹²B. Ramachandran, J. Senekowitsch, and R. E. Wyatt, *Chem. Phys. Lett.* **270**, 387 (1997).
- ¹³F. B. Brown and D. G. Truhlar, *Chem. Phys. Lett.* **117**, 307 (1985).
- ¹⁴T. C. Allison, B. Ramachandran, J. Senekowitsch, D. G. Truhlar, and R. E. Wyatt, *J. Mol. Struct.: THEOCHEM* **454**, 307 (1998).
- ¹⁵B. Ramachandran, E. A. Schrader, III, J. Senekowitsch, and R. E. Wyatt, *J. Chem. Phys.* **111**, 3862 (1999).

- ¹⁶D. J. Rakestraw, K. G. McKendrick, and R. N. Zare, *J. Chem. Phys.* **87**, 7341 (1987); R. Zhang, W. J. van der Zande, M. J. Bronikowski, and R. N. Zare, *ibid.* **94**, 2704 (1991).
- ¹⁷B. Ramachandran, *J. Chem. Phys.* **112**, 3680 (2000).
- ¹⁸L. Wang, C. Kalyanaraman, and A. B. McCoy, *J. Chem. Phys.* **110**, 11221 (1999).
- ¹⁹S. Skokov, T. Tsuchida, S. Nanbu, J. M. Bowman, and S. K. Gray, *J. Chem. Phys.* (to be published).
- ²⁰V. Piermarini, F. Gogtas, A. Lagana, and G. G. Balint-Kurti (unpublished).
- ²¹J. M. Bowman, *J. Phys. Chem.* **95**, 4960 (1991).
- ²²D. H. Zhang, J. C. Light, and S.-Y. Lee, *J. Chem. Phys.* **109**, 79 (1998); D. H. Zhang and J. Z. H. Zhang, *ibid.* **110**, 7622 (1999).
- ²³J. M. Bowman and H. M. Shnider, *J. Chem. Phys.* **110**, 4428 (1999).
- ²⁴K. Nobusada and H. Nakamura, *J. Phys. Chem. A* **103**, 6715 (1999).
- ²⁵O. I. Tolstikhin, S. Watanabe, and M. Matsuzawa, *J. Phys. B* **29**, L389 (1996).
- ²⁶K. L. Baluja, P. G. Burke, and L. A. Morgan, *Comput. Phys. Commun.* **27**, 299 (1982).
- ²⁷M. B. Faist, J. T. Muckerman, and F. E. Schubert, *J. Chem. Phys.* **69**, 4087 (1978).
- ²⁸D. G. Truhlar and J. T. Muckerman, in *Atom-Molecule Collision Theory: A Guide to the Experimentalist*, edited by R. B. Bernstein (Plenum, New York, 1979).
- ²⁹D. L. Bunker, *Methods Comput. Phys.* **10**, 287 (1971). The error in Eq. (16) of this work has been corrected in the present calculations.
- ³⁰F. J. Aoiz, L. Bañares, J. F. Castillo, M. Menéndez, and J. E. Verdasco, *Phys. Chem. Chem. Phys.* **1**, 1149 (1999).
- ³¹C. Zhu, H. Nakamura, and K. Nobusada, *Phys. Chem. Chem. Phys.* **2**, 557 (2000).
- ³²R. D. H. Brown and I. W. M. Smith, *Int. J. Chem. Kinet.* **7**, 301 (1975).
- ³³W. Hack, G. Mex, and H. G. Wagner, *Ber. Bunsenges. Phys. Chem.* **81**, 677 (1977).
- ³⁴D. L. Singleton and R. J. Cvetanović, *Int. J. Chem. Kinet.* **13**, 945 (1981).
- ³⁵K. Mahmud, J.-S. Kim, and A. Fontijn, *J. Phys. Chem.* **94**, 2994 (1990).

Journal of Chemical Physics is copyrighted by AIP Publishing LLC (AIP). Reuse of AIP content is subject to the terms at: <http://scitation.aip.org/termsconditions>. For more information, see <http://publishing.aip.org/authors/rights-and-permissions>.